



## Steady-state fracture toughness of elastic-plastic solids: Isotropic versus kinematic hardening

Juul, K. J.; Martínez Pañeda, E.; Nielsen, K.L.; Niordson, C. F.

*Published in:*  
Engineering Fracture Mechanics

*Link to article, DOI:*  
[10.1016/j.engfracmech.2018.12.016](https://doi.org/10.1016/j.engfracmech.2018.12.016)

*Publication date:*  
2019

*Document Version*  
Peer reviewed version

[Link back to DTU Orbit](#)

*Citation (APA):*  
Juul, K. J., Martínez Pañeda, E., Nielsen, K. L., & Niordson, C. F. (2019). Steady-state fracture toughness of elastic-plastic solids: Isotropic versus kinematic hardening. *Engineering Fracture Mechanics*, 207, 254-268. <https://doi.org/10.1016/j.engfracmech.2018.12.016>

---

### General rights

Copyright and moral rights for the publications made accessible in the public portal are retained by the authors and/or other copyright owners and it is a condition of accessing publications that users recognise and abide by the legal requirements associated with these rights.

- Users may download and print one copy of any publication from the public portal for the purpose of private study or research.
- You may not further distribute the material or use it for any profit-making activity or commercial gain
- You may freely distribute the URL identifying the publication in the public portal

If you believe that this document breaches copyright please contact us providing details, and we will remove access to the work immediately and investigate your claim.

# Steady-state fracture toughness of elastic-plastic solids: Isotropic versus kinematic hardening

K. J. Juul<sup>a,\*</sup>, E. Martínez-Pañeda<sup>b</sup>, K. L. Nielsen<sup>a</sup>, C. F. Niordson<sup>a</sup>

<sup>a</sup>*Department of Mechanical Engineering, Solid Mechanics, Technical University of Denmark, DK-2800 Kgs. Lyngby, Denmark*

<sup>b</sup>*Department of Engineering, Cambridge University, CB2 1PZ Cambridge, UK*

---

## Abstract

The fracture toughness for a mode I/II crack propagating in a ductile material has been subject to numerous investigations. However, the influence of the material hardening law has received very limited attention, with isotropic hardening being the default choice if cyclic loads are absent. The present work extends the existing studies of monotonic mode I/II steady-state crack propagation with the goal to compare the predictions from an isotropic hardening model with that of a kinematic hardening model. The work is conducted through a purpose-built steady-state framework that directly delivers the steady-state solution. In order to provide a fracture criterion, a cohesive zone model is adopted and embedded at the crack tip in the steady-state framework, while a control algorithm for the far-field, that significantly reduces the number of equilibrium iterations is employed to couple the far-field loading to the correct crack tip opening. Results show that the steady-state fracture toughness (shielding ratio) obtained for a kinematic hardening material is larger than for the corresponding isotropic hardening case. The difference between the isotropic and kinematic model is tied to the non-proportional loading conditions and reverse plasticity. This also explains the vanishing difference in the shielding ratio when considering mode II crack propagation as the non-proportional loading is less pronounced and the reverse plasticity is absent.

*Keywords:* Steady-state, Isotropic hardening, Kinematic hardening, Active plastic zone, Shielding ratio

---

\*Corresponding author

*Email address:* krjoju@mek.dtu.dk (K. J. Juul)

---

1 **1. Introduction**

2 The influence of plastic deformation on fracture toughness has been the  
3 motivation of a large number of studies in the literature (see e.g. Varias and Shih [1],  
4 Tvergaard and Hutchinson [2], Suo et al. [3], Cleveringa et al. [4], Tver-  
5 gaard [5], Nielsen et al. [6], Nielsen and Niordson [7], Jiang et al. [8], Juul et al. [9].  
6 The common goal has been to achieve a better understanding of the under-  
7 lying mechanics that affect the toughness of ductile materials by gaining  
8 insight into the role of crack tip plasticity. Factors such as rate-dependency  
9 (Landis et al. [10]), work hardening (Tvergaard and Hutchinson [11]), strain  
10 gradients (Wei and Hutchinson [12], Martínez-Pañeda and Niordson [13]),  
11 dynamic lattice effects (Freund and Hutchinson [14]), material property mis-  
12 match (Cao and Evans [15], Tvergaard [16]), or micro structure evolution  
13 (Kumar and Curtin [17]) affect the fracture properties and determine the  
14 extent of crack propagation.

15 Except for the recent study of mode I cracks by Martínez-Pañeda and Fleck [18],  
16 the majority of the published studies of crack growth under monotonic load-  
17 ing confine their focus to isotropic hardening materials, despite the crucial  
18 impact of the plastic material response on the shielding ratio. In fact, plas-  
19 tic deformation and the associated dissipation of energy is known to be the  
20 main contributor towards enhancing the fracture resistance beyond crack ini-  
21 tiation. The far-field loading drives this process and despite being monotonic  
22 at the far boundary the conditions experienced by the material passing by  
23 the crack tip are very different. It is well documented that material entering  
24 the active plastic zone near a steadily growing mode I crack will either exit  
25 into an unloading wake or experience reverse plastic loading close to the new  
26 fracture surface. Thus, any Bauschinger effect originating from kinematic  
27 hardening must have an important influence. Though reversed plasticity  
28 does not take place in mode II crack growth, non-proportional loading for  
29 material at a distance from the crack face will be demonstrated in the results  
30 of the present study. The present study is further motivated by the fact  
31 that kinematic hardening effects are expected to play an increasing role in  
32 modern structural materials. Composite, multiphase or refined microstruc-  
33 tures influence the work hardening response, enhancing kinematic hardening  
34 (Ashby [19], de Formanoir et al. [20]).

35 The main goal of the present study is to investigate how the choice of

36 hardening model influences the fracture toughness of a steadily growing crack  
37 under monotonic mode I, mode II, and mixed mode I/II far-field condi-  
38 tions. In plate tearing steadily growing cracks are encountered when the  
39 crack has propagated multiple plate thicknesses. In fact, steady-state is typ-  
40 ically reached after crack growth on the order of seven plate thicknesses  
41 (Woelke et al. [21], Andersen et al. [22]). Hence, this state can dominate a  
42 significant part of the crack path in shell-like structures such as ships, air  
43 planes, and cars. To focus the effort on the part of the propagation path  
44 taking place under steady-state conditions, the framework first proposed by  
45 Dean and Hutchinson [23] has been adopted and extended to kinematic hard-  
46 ening plasticity. The material steady-state fracture toughness, composed by  
47 the energy going into material separation as-well as energy dissipated in  
48 the surrounding material, is evaluated by introducing the cohesive traction-  
49 separation relation proposed by Tvergaard and Hutchinson [2]. This allows  
50 for an analysis of the ratio between the external energy applied to the system  
51 and the energy specified for the fracture process (referred to as the shield-  
52 ing ratio). Attention is focused on the change in fracture properties when  
53 shifting from isotropic hardening to kinematic hardening. Thus, the stress  
54 evolution for material points in the vicinity of the crack tip is of particular  
55 interest as any deviation from proportional loading will be treated differently  
56 in the two types of hardening models.

57 Throughout this paper, the two types of material hardening and their  
58 differences are studied for various conditions of the near tip fracture process  
59 (in terms of cohesive zone parameters). Furthermore, the origin of these dif-  
60 ferences is traced by mapping out the energy dissipation in the vicinity of  
61 the propagating crack. In the present study, the material is assumed to be  
62 governed by linear hardening. This is chosen to ensure a constant tangent  
63 modulus, thus clearly bringing out the essential differences in predictions for  
64 steady-state fracture toughness between the isotropic and kinematic harden-  
65 ing models.

66 The paper is divided into the following sections: The modified boundary  
67 value problem is presented in Section 2, the material model, interface model,  
68 the algorithm controlling the far-field loading, and the numerical formulation  
69 are presented in Section 3, the results are presented in Section 4, and lastly  
70 some concluding remarks are stated in Section 5. Throughout, index nota-  
71 tion, including Einstein's summation convention, is used and a superimposed  
72 dot,  $(\dot{\phantom{x}})$ , denotes the time derivative.

73 **2. Mixed mode boundary layer problem**

The steady-state crack propagation study is carried out for mode I/II loading conditions under the assumption of small-scale yielding. To model the continuously growing crack, the steady-state framework presented by Dean and Hutchinson [23] is coupled with a cohesive zone description of fracture, employing the traction-separation law proposed by Tvergaard and Hutchinson [2]. The problem, commonly known as the modified boundary layer problem, is modeled in a 2D plane strain setting as illustrated in Fig. 1 (the considered material properties are collected in Tab. 1). The domain is constructed large enough such that boundary effects do not affect the solution, and the stress intensity factors,  $K_I$  and  $K_{II}$ , can be employed to characterize the stress-field. The mode I/II loading condition is imposed as a far-field condition according to the elastic solution presented by Williams [24] and dictates that the stress field has the form;

$$\sigma_{ij} = \frac{1}{\sqrt{2\pi r}} \left( K_I f_{ij}^I(r, \theta) + K_{II} f_{ij}^{II}(r, \theta) \right), \quad (1)$$

74 where  $r$  and  $\theta$  are polar coordinates related to the crack tip position,  $f_{ij}(r, \theta)$   
 75 are dimensionless mode functions, and  $K_I$  and  $K_{II}$  are the stress intensity  
 76 factors representing the mode I and II contributions, respectively. Through-  
 77 out this work, it is assumed that the crack propagates in a straight line (along  
 78 the  $x_1$ -direction in Fig. 1). This assumption, common to other mixed-mode  
 79 crack propagation analyses (see e.g. Tvergaard [5]), constitutes an approxi-  
 80 mation under mode II dominated loading conditions.

The steady-state fracture toughness is quantified by the so-called crack tip shielding ratio,  $K_{ss}/K_0$ , which is the stress intensity factor for steady-state crack growth,  $K_{ss}$ , normalized by the stress intensity factor for crack initiation,  $K_0$ . The reference stress intensity factor,  $K_0$ , is defined as;

$$K_0 = \sqrt{\frac{E\Gamma_0}{1-\nu^2}} \quad (2)$$

where  $E$  is Young's modulus,  $\nu$  is Poisson's ratio, and  $\Gamma_0$  is the fracture energy (work of separation of the cohesive zone model). Moreover, any length quantity in the present study is normalized by the reference plastic zone size,

$R_0$ ;

$$R_0 = \frac{1}{3\pi} \left( \frac{K_0}{\sigma_y} \right)^2 \quad (3)$$

81 where  $\sigma_y$  is the initial yield stress of the material.

### 82 **3. Constitutive relations and modeling**

#### 83 *3.1. Traction-separation relation*

The traction-separation relation employed is adopted from Tvergaard and Hutchinson [11, 2]. Accordingly, the traction energy potential is defined as;

$$\Phi(\delta_t, \delta_n) = \delta_n^c \int_0^\lambda \sigma(\lambda') d\lambda' \quad (4)$$

where  $\sigma(\lambda)$  is the traction shown in Fig. 2 as a function of the non-dimensional measure of separation,  $\lambda$ . The non-dimensional crack separation is defined as;  $\lambda = \sqrt{(\delta_n/\delta_n^c)^2 + (\delta_t/\delta_t^c)^2}$ , where  $\delta_n$  and  $\delta_t$  denote the actual separation in the normal and tangential directions, respectively, and the quantities with superscript  $c$  denote the corresponding critical values. Thus, as illustrated in Fig. 2, the bond between two nodes completely breaks at  $\lambda = 1$ . From the traction energy potential, the normal and tangential tractions in the fracture process zone are given as;

$$T_n = \frac{\partial \Phi}{\partial \delta_n} = \frac{\sigma(\lambda)}{\lambda} \frac{\delta_n}{\delta_n^c} \quad \text{and} \quad T_t = \frac{\partial \Phi}{\partial \delta_t} = \frac{\sigma(\lambda)}{\lambda} \frac{\delta_n^c}{\delta_t^c} \frac{\delta_t}{\delta_t^c}. \quad (5)$$

Finally, the work of separation per unit area of interface (the fracture energy) is defined as;

$$\Gamma_0 = \frac{1}{2} \hat{\sigma} \delta_n^c (1 - \lambda_1 + \lambda_2) \quad (6)$$

84 where  $\hat{\sigma}$  denotes the peak traction (cohesive strength) shown in Fig. 2.

#### 85 *3.2. Constitutive models*

86 The framework relies on an infinitesimal strain formulation (both for the  
87 isotropic and kinematic model). The small strain formulation has been cho-

88 sen because previous finite strains studies have shown that the crack prop-  
 89 agates at relatively small deformations (Tvergaard and Hutchinson [11]) for  
 90 the selected values of the cohesive strength. This is also seen in the work by  
 91 e.g., Wei and Hutchinson [12], Martínez-Pañeda and Fleck [18] where finite  
 92 strain results are precisely reproduce by a small strain framework. In the  
 93 infinitesimal strain formulation, the total strains,  $\varepsilon_{ij}$ , are determined from  
 94 the displacement gradients;  $\varepsilon_{ij} = (u_{i,j} + u_{j,i})/2$ . The total strains consist  
 95 of an elastic part,  $\varepsilon_{ij}^e$ , and plastic part,  $\varepsilon_{ij}^p$ , which for an additive split gives  
 96 the following relationship;  $\varepsilon_{ij} = \varepsilon_{ij}^e + \varepsilon_{ij}^p$ . Subsequently, the stress field in  
 97 the rate-independent model is determined from the tensor of instantaneous  
 98 moduli,  $L_{ijkl}$ , and the total strain as;

$$\dot{\sigma}_{ij} = L_{ijkl}\dot{\varepsilon}_{kl}. \quad (7)$$

99 Throughout this work, the material behavior is assumed to be governed  
 100 by linear hardening such that the tangent modulus,  $E_t$ , remains constant and  
 101 given as a fraction of Young's modulus,  $E$ . The tangent modulus,  $E_t$ , enters  
 102 the instantaneous moduli,  $L_{ijkl}$ , in Eq. (21).

### 103 3.2.1. Isotropic hardening

The isotropic model does not consider the Bauschinger effect, as the yield surface expands isotropically in all directions (see Fig. 3a) while maintaining its origin in stress space. The von Mises yield criterion, employed in the present study, takes the form

$$F(\sigma_{ij}) = \frac{3}{2}s_{ij}s_{ij} - (\sigma_e)_{\max}^2 = 0, \quad (8)$$

104 where  $s_{ij}$  is the deviatoric stress and  $\sigma_e$  is the von Mises stress. In the context  
 105 of an incremental formulation, the active plastic zone can be evaluated by  
 106 integrating the total stress in time (Eq. (7)), followed by an evaluation of the  
 107 criterion for plasticity;

$$\beta = \begin{cases} 1, & \text{for } \sigma_e = (\sigma_e)_{\max} \text{ and } \dot{\sigma}_e \geq 0 \\ 0, & \text{for } \sigma_e < (\sigma_e)_{\max} \text{ or } \dot{\sigma}_e < 0 \end{cases}$$

108 where  $\beta = 1$  indicates a material point governed by plastic loading and  $\beta = 0$   
 109 indicates a material point governed by elastic unloading (applied in Eq. (21)).

110 *3.2.2. Kinematic hardening*

For kinematic hardening, where the yield surface translates in stress space (see Fig. 3b), the yield condition reads;

$$F(\sigma_{ij}, \alpha_{ij}) = \frac{3}{2} \tilde{\sigma}_{ij} \tilde{\sigma}_{ij} - (\sigma_y)^2 = 0, \quad (9)$$

111 where symbols with ( $\tilde{\phantom{x}}$ ) denote stress quantities related to the local origin of  
 112 the translating yield surface, representing the well-known Bauschinger effect.  
 113 The origin of the translating yield surface, tracked through the back stress,  
 114  $\alpha_{ij}$ , is used to establish the local stress;

$$\tilde{\sigma}_{ij} = \sigma_{ij} - \alpha_{ij} \quad (10)$$

in the yield function, Eq. (9), through the deviatoric stress,  $\tilde{\sigma}_{ij}$ . The translation of the yield surface is modeled through an evolution law. Several evolution laws exist in the literature, ranging from simple models to very sophisticated models including effects such as ratchetting and shakedown (Lemaitre and Chaboche [25]). For fracture problems under monotonic loading, reversed loading is expected in the wake of the leading active plastic zone, but repeated cyclic loading is not taking place which means that ratchetting and shakedown are not relevant to the present study. Consequently, the well-known evolution law by Ziegler [26] is chosen, as it includes all the necessary features. Thus, the back stress evolves as;

$$\dot{\alpha}_{ij} = (\sigma_{ij} - \alpha_{ij}) \dot{\mu} \quad (11)$$

115 where  $\dot{\mu}$  is a proportionality coefficient which is defined as;

$$\dot{\mu} = \frac{3}{2} \frac{\dot{\sigma}_{ij} \tilde{\sigma}_{ij}}{\sigma_y^2} \quad (12)$$

116 in the present study. For kinematic hardening, where the yield surface trans-  
 117 lates but maintain its size, the criterion for plasticity is therefore evaluated  
 118 according to;

$$\beta = \begin{cases} 1, & \text{for } \tilde{\sigma}_e = \sigma_y \text{ and } \tilde{\sigma}_{kl} \dot{\sigma}_{kl} \geq 0 \\ 0, & \text{for } \tilde{\sigma}_e < \sigma_y \text{ or } \tilde{\sigma}_{kl} \dot{\sigma}_{kl} < 0 \end{cases},$$

119 *3.3. Steady-state framework*

120 The fracture toughness at steady-state,  $K_{ss}$ , can be approximated with  
 121 traditional incremental numerical methods by computing the crack growth  
 122 resistance curve. However, such methods often suffer from convergence issues  
 123 and are inefficient as they are forced through the transient regime of a prob-  
 124 lem before reaching the steady-state. To avoid such issues, a steady-state  
 125 framework is employed, leading to accurate predictions of the steady-state  
 126 fracture toughness at a fraction of the computational cost. The steady-state  
 127 framework presented builds upon an extension of the procedure suggested by  
 128 Dean and Hutchinson [23] to account for a kinematic hardening law.

129 The pivotal step is to utilize the nature of a steady-state problem to  
 130 determine the history dependent field quantities. The steady-state condition  
 131 is noticed for an observer located at the tip of a continuously growing crack  
 132 when the field quantities that surrounds the crack tip are no longer subject to  
 133 changes. Any time derived quantity,  $\dot{f}$ , in the constitutive equations are then  
 134 transformed into spatial derivatives, through the crack propagation speed,  
 135  $\dot{a}$ , in the direction of the material flow (negative  $x_1$ -direction, see Fig. 1)  
 136 according to the relation;

$$\dot{f} = -\dot{a} \frac{\partial f}{\partial x_1}. \quad (13)$$

137 Thus, any total quantity at a given material point  $(x_1^*, x_2^*)$ , is evaluated  
 138 through spatial integration, starting upstream in the undeformed elastic ma-  
 139 terial ahead of the crack tip  $(x_1^0, x_2^*)$ , and following a streamline (material  
 140 flow line) until it reaches the point of interest  $(x_1^*, x_2^*)$  downstream (see e.g.  
 141 Juul et al. [9, 27]). Thus, the loading history at a given material point  $(x_1^*, x_2^*)$   
 142 is retrieved from all the upstream points along the streamline, representing  
 143 earlier states.

144 The steady-state framework is based on the conventional principle of vir-  
 145 tual work (PWW) for quasi-static problems;

$$\int_V \mathcal{L}_{ijkl} \varepsilon_{kl} \delta \varepsilon_{ij} dV + \int_{S_c} T_i \delta u_i dS_c = \int_S t_i \delta u_i dS + \int_V \mathcal{L}_{ijkl} \varepsilon_{kl}^p \delta \varepsilon_{ij} dV \quad (14)$$

146 where  $t_i = \sigma_{ij} n_j$  is the surface traction,  $T_i$  is the traction from the traction-  
 147 separation law, and  $\mathcal{L}_{ijkl}$  is the isotropic elastic stiffness tensor. The volume  
 148 analyzed is denoted  $V$ ,  $S_c$  is the interface (cohesive) surface, and  $S$  is the  
 149 bounding surface, with  $n_j$  denoting the unit outward normal vector.

150 The algorithm employed for the spatial integration procedure is outlined

151 below, where it is seen that the main difference is in the integration of the  
 152 back stress in step 4 ( $m$  refers to the iteration number):

- 153 1. Use the plastic strains,  $\varepsilon_{ij}^{p(m-1)}$ , to determine the current displacement  
 154 field,  $u_i^{(m)}$  ( $\varepsilon_{ij}^{p(m-1)}$  is assumed to be zero in the first iteration).
- 155 2. Determine the total strain,  $\varepsilon_{ij}^{(m)}$ , from the displacement field,  $u_i^{(m)}$ .
- 156 3. Determine the total stress field outside the streamline domain:
  - (i) Stresses can be determined directly from the total strain ( $\varepsilon_{ij}^{p(m)} = 0$ ):

$$\sigma_{ij}^{(m)} = \mathcal{L}_{ijkl} \varepsilon_{kl}^{(m)} \quad (15)$$

157 where  $\mathcal{L}_{ijkl}$  is the elastic stiffness tensor.

- 158 4. Determine the stresses inside the streamline domain:
  - (i) Determine the spatial derivative of the stress:

$$\frac{\partial \sigma_{ij}^{(m)}}{\partial x_1} = L_{ijkl}^{(m)} \frac{\partial \varepsilon_{kl}^{(m)}}{\partial x_1} \quad (16)$$

159 where  $L_{ijkl}$  is the tensor of instantaneous moduli.

- (ii) Determine the spatial derivative of the back stress (only for kinematic hardening):

$$\frac{\partial \alpha_{ij}^{(m)}}{\partial x_1} = (\sigma_{ij} - \alpha_{ij}) \frac{\partial \mu^{(m)}}{\partial x_1} \quad \text{with} \quad \frac{\partial \mu^{(m)}}{\partial x_1} = \frac{3 \tilde{s}_{ij}}{2 \sigma_y^2} \frac{\partial \sigma_{ij}^{(m)}}{\partial x_1} \quad (17)$$

- (iii) Perform spatial integration along streamlines:

$$\sigma_{ij}^{(m)} = \int_{x_1^0}^{x_1^*} \frac{\partial \sigma_{ij}^{(m)}}{\partial x_1} dx_1 \quad \text{and} \quad \alpha_{ij}^{(m)} = \int_{x_1^0}^{x_1^*} \frac{\partial \alpha_{ij}^{(m)}}{\partial x_1} dx_1 \quad (18)$$

- 160 5. Determine the plastic strain field,  $\varepsilon_{ij}^{p(m)} = \varepsilon_{ij}^{(m)} - \mathcal{M}_{ijkl} \sigma_{kl}^{(m)}$ , in the  
 161 streamline domain, with  $\mathcal{M}_{ijkl}$  being the elastic compliance tensor.
- 162 6. Repeat 1 to 5 until solution is converged.

In the algorithm, the following constitutive tensors have been applied

which include the elastic stiffness tensor,

$$\mathcal{L}_{ijkl} = \frac{E}{1 + \nu} \left[ \frac{1}{2}(\delta_{ik}\delta_{jl} + \delta_{il}\delta_{jk}) + \frac{\nu}{1 - 2\nu}\delta_{ij}\delta_{kl} \right], \quad (19)$$

the elastic compliance tensor,

$$\mathcal{M}_{ijkl} = \frac{1}{E} \left[ \frac{1 + \nu}{2}(\delta_{ik}\delta_{jl} + \delta_{il}\delta_{jk}) - \nu\delta_{ij}\delta_{kl} \right], \quad (20)$$

and the isotropic tensor of instantaneous moduli,

$$L_{ijkl} = \mathcal{L}_{ijkl} - \beta \frac{3}{2} \frac{E/E_t - 1}{E/E_t - (1 - 2\nu)/3} \frac{s_{ij}s_{kl}}{\sigma_e^2}, \quad (21)$$

163 where it should be noted that in the tensor of instantaneous moduli,  $s_{ij}s_{kl}/\sigma_e^2$   
 164 is substituted with  $\tilde{s}_{ij}\tilde{s}_{kl}/\sigma_y^2$  for the kinematic hardening model.

165 The numerical stability of the steady-state algorithm is in general bet-  
 166 ter than for incremental frameworks, although, certain problems can arise  
 167 in areas with steep gradients such as at the crack tip. In order to limit  
 168 such stability issue of the algorithm a minor change has been made to the  
 169 original procedure by Dean and Hutchinson [23] following the suggestion by  
 170 Niordson [28] and Nielsen and Niordson [7], where a sub-increment procedure  
 171 between Gauss points has been introduced in the spatial integration scheme.

#### 172 3.4. Cohesive elements and traction-separation relation

The implementation of the cohesive zone builds upon the standard case presented by e.g. del Busto et al. [29]. However, for the steady-state framework, minor modifications are introduced when building both the stiffness matrix and the right-hand side of the equation system. When discretizing the virtual work principle in Eq. (14), the nonlinear part of the contribution from the cohesive elements is moved to the right-hand side and acts as a force term. Hence, the discretized system reads;

$$\begin{aligned} & \left( \int_V [B]^T [\mathcal{L}] [B] dV + \int_{S_c} [B_c]^T \frac{\partial \{T^{\text{ini}}\}}{\partial \{\delta\}} [B_c] dS_c \right) \{U\} \\ & = \int_S [N]^T \{t\} dS + \int_V [B]^T [\mathcal{L}] \{\varepsilon^p\} dV + \int_V [B_c]^T (\{T^{\text{lin}}\} - \{T^{\text{act}}\}) dS_c \end{aligned} \quad (22)$$

173 where  $\partial\{T^{\text{ini}}\}/\partial\{\delta\}$  is the initial slope of the traction-separation curve in  
 174 the region  $\lambda < \lambda_1$  (see Fig. 2),  $T_i^{\text{lin}}$  is the corresponding traction predicted  
 175 if a linear curve with the initial slope is followed, and  $T_i^{\text{act}}$  is the traction  
 176 obtained from the actual curve in Fig. 2. The standard strain-displacement  
 177 and shape function matrices,  $[B]$ ,  $[B_c]$  and  $[N]$ , are given in the work by del  
 178 Busto et al. [29]. The partition of the cohesive contribution is necessary for  
 179 the steady-state framework because the equations are no longer expressed  
 180 on incremental form. However, the partition also entails a considerable re-  
 181 duction in the computational cost as the system matrix only needs to be  
 182 built and factorized once, with subsequent iterations relying solely on back-  
 183 substitution.

184 In the present study, the equation system is discretized using quadratic  
 185 8-node isoparametric elements evaluated through  $2 \times 2$  Gauss points and  
 186 quadratic 6-node isoparametric cohesive elements evaluated through 8 Gauss  
 187 points.

### 188 *3.5. Control algorithm for the boundary layer problem*

189 The far-field required to drive crack propagation in an elastic-plastic solid  
 190 is generally unknown and, thus, to efficiently study the steady-state fracture  
 191 toughness (the shielding ratio) it is necessary to implement a scheme to  
 192 control the applied far-field loading such that the energy needed for steady-  
 193 state crack propagation is provided. For this purpose, several techniques have  
 194 been proposed in the literature. In the present study, the idea employed by  
 195 Segurado and LLorca [30] and Martínez-Pañeda and Fleck [31] is adopted  
 196 as it offers fast and stable convergence while at the same time lending itself  
 197 nicely to implementation in the developed numerical scheme. The technique  
 198 is here generalized to treat problems with mode mixity. The key idea behind  
 199 the procedure is to link the loading history to a monotonically increasing  
 200 parameter that is not affected by potential instabilities. For the present  
 201 investigation of steady-state crack growth such a parameter could be the  
 202 crack tip opening displacements (normal and tangential separation) as such  
 203 quantities should be non-decreasing at all times during loading - or, more  
 204 precisely, kept fixed in the steady-state framework (schemes with other or  
 205 more parameters included can also be found in Segurado and LLorca [30]).

Once suitable monotonically increasing parameters have been chosen, a  
 connection between these parameters and the load at the outer far boundary  
 must be established. The connection is introduced through; i) two constraint  
 equations (see Eq. (23)) that ensure the prescribed crack tip opening, ii) a

global equilibrium equation which ensures that the loading on the crack tip, enforced by the constraint equations, is balanced out by the loading on the outer far boundary, and iii) a set of geometrical constraints that ensure a smooth distribution of the far-field loading according to the elastic solution by Williams [24]. The two additional constraint equations are introduced by adding two additional degrees of freedom,  $Q_n$  and  $Q_t$ , to the system (with corresponding right-hand sides,  $\Delta_n$  and  $\Delta_t$ ). The desired crack tip opening,  $\Delta_n$  and  $\Delta_t$ , is then enforced through the following displacement constraints;

$$u_1^{(N_1)} - u_1^{(N_2)} = \Delta_t \quad \text{and} \quad u_2^{(N_2)} - u_2^{(N_1)} = \Delta_n, \quad (23)$$

206 where  $N_1$  and  $N_2$  refers to the two nodes located at the crack tip on each  
 207 side of the crack plane (see Fig. 4). In the case of a pure mode I loaded  
 208 crack, the enforced tip displacements are;  $\Delta_n = \delta_n^c$  and  $\Delta_t = 0$ , while the  
 209 pure mode II crack is analyzed by enforcing;  $\Delta_n = 0$  and  $\Delta_t = \delta_t^c$ . Here,  $\delta_n^c$   
 210 and  $\delta_t^c$  are the critical normal and tangential separation, respectively, related  
 211 to the cohesive traction-separation relation (see Section 3.4).

The constraint equations in Eq. (23) introduce reaction forces at the crack tip that drive the opening. This is, however, artificial and does not resemble crack growth under far-field mode I/II loading. To ensure proper far-field loading of the crack tip, a coupling to the outer far boundary is created through two global equilibrium considerations such that the reaction force at the crack tip becomes zero. This is enforced by adding the following contributions to the system matrix,  $K$ , for a given node  $m$ ;

$$K((N_{BC})_1, m)u^{(m)} + Q_t = 0 \quad (24)$$

$$K((N_{BC})_2, m)u^{(m)} + Q_n = 0 \quad (25)$$

where  $(N_{BC})_i$  refers to the global degrees of freedom of an arbitrary node,  $N_{BC}$ , on the outer far boundary (see Fig. 4). The coupling ensures that the chosen node on the far boundary,  $N_{BC}$ , will displace according to the prescribed crack tip opening, as dictated by equilibrium, i.e. the far-field becomes an outcome of the equilibrium solution. Finally, a set of geometric constraints are defined to ensure that the displacement of all the nodes at the outer boundary is consistent with the displacements of the arbitrary node,  $N_{BC}$ . The geometric constraint is determined from the elastic far-field solution to the boundary layer problem presented in Section 2. In terms of the displacement field, the elastic far-field of node  $m$ , at the outer far

boundary, reads;

$$\begin{aligned} u_1^{(m)}(r(m), \theta(m)) &= C_{(m)}(K_I f_{K_I}^{u_1^{(m)}}(r(m), \theta(m)) + K_{II} f_{K_{II}}^{u_1^{(m)}}(r(m), \theta(m))) \\ u_2^{(m)}(r(m), \theta(m)) &= C_{(m)}(K_I f_{K_I}^{u_2^{(m)}}(r(m), \theta(m)) - K_{II} f_{K_{II}}^{u_2^{(m)}}(r(m), \theta(m))) \end{aligned} \quad (26)$$

where  $C_m = 1/(2\mu)\sqrt{r(m)/(2\pi)}$  and  $f$  are displacement mode functions. Thus, the stress intensity factors,  $K_I$  and  $K_{II}$ , corresponding to a known displacement,  $u_i^{(m)}$ , of a given node,  $m$ , on the outer far boundary can be determined by inverting Eq. (26), such that;

$$\begin{aligned} K_I &= \frac{f_{K_{II}}^{u_2^{(m)}} u_1^{(m)} + f_{K_{II}}^{u_1^{(m)}} u_2^{(m)}}{C_{(m)}(f_{K_{II}}^{u_1^{(m)}} f_{K_I}^{u_2^{(m)}} + f_{K_{II}}^{u_2^{(m)}} f_{K_I}^{u_1^{(m)}})} \\ K_{II} &= -\frac{f_{K_I}^{u_2^{(m)}} u_1^{(m)} - f_{K_I}^{u_1^{(m)}} u_2^{(m)}}{C_{(m)}(f_{K_{II}}^{u_1^{(m)}} f_{K_I}^{u_2^{(m)}} + f_{K_{II}}^{u_2^{(m)}} f_{K_I}^{u_1^{(m)}})} \end{aligned} \quad (27)$$

That is, the  $K$ -field applied to the outer far boundary can be linked to the displacement of the arbitrary node,  $N_{BC}$ , and subsequently to the remaining nodes on the outer far boundary. In this way, the multi-point geometric constraint is stated as;

$$\begin{aligned} u_1^{(m)} - \frac{C_{(m)}}{C_{(N_{BC})}} \frac{f_{K_{II}}^{u_1^{(m)}} f_{K_I}^{u_2^{(N_{BC})}} + f_{K_I}^{u_1^{(m)}} f_{K_{II}}^{u_2^{(N_{BC})}}}{f_{K_{II}}^{u_1^{(N_{BC})}} f_{K_I}^{u_2^{(N_{BC})}} + f_{K_{II}}^{u_2^{(N_{BC})}} f_{K_I}^{u_1^{(N_{BC})}}} u_1^{(N_{BC})} \\ - \frac{C_{(m)}}{C_{(N_{BC})}} \frac{f_{K_I}^{u_1^{(m)}} f_{K_{II}}^{u_1^{(N_{BC})}} - f_{K_{II}}^{u_1^{(m)}} f_{K_I}^{u_1^{(N_{BC})}}}{f_{K_{II}}^{u_1^{(N_{BC})}} f_{K_I}^{u_2^{(N_{BC})}} + f_{K_{II}}^{u_2^{(N_{BC})}} f_{K_I}^{u_1^{(N_{BC})}}} u_2^{(N_{BC})} = 0 \\ u_2^{(m)} - \frac{C_{(m)}}{C_{(N_{BC})}} \frac{f_{K_I}^{u_2^{(m)}} f_{K_{II}}^{u_2^{(N_{BC})}} - f_{K_{II}}^{u_2^{(m)}} f_{K_I}^{u_2^{(N_{BC})}}}{f_{K_{II}}^{u_1^{(N_{BC})}} f_{K_I}^{u_2^{(N_{BC})}} + f_{K_{II}}^{u_2^{(N_{BC})}} f_{K_I}^{u_1^{(N_{BC})}}} u_1^{(N_{BC})} \\ - \frac{C_{(m)}}{C_{(N_{BC})}} \frac{f_{K_I}^{u_2^{(m)}} f_{K_{II}}^{u_1^{(N_{BC})}} + f_{K_{II}}^{u_2^{(m)}} f_{K_I}^{u_1^{(N_{BC})}}}{f_{K_{II}}^{u_1^{(N_{BC})}} f_{K_I}^{u_2^{(N_{BC})}} + f_{K_{II}}^{u_2^{(N_{BC})}} f_{K_I}^{u_1^{(N_{BC})}}} u_2^{(N_{BC})} = 0 \end{aligned} \quad (28)$$

213 matrix. In combination with the constraint equation in Eq. (23) this ensures  
214 a distributed loading on the outer far boundary according to the  $K$ -field  
215 required to enforce the prescribed crack tip displacements ( $\Delta_n$  and  $\Delta_t$ ).

## 216 4. Results

217 Two types of analyses are conducted to gain better insight into how the  
218 hardening model affects the fracture toughness at steady-state crack growth  
219 in an elastic-plastic solid. First, the shielding ratio,  $K_{ss}/K_0$ , for various frac-  
220 ture process zone conditions (controlled by the cohesive zone) is investigated  
221 to quantify the differences between isotropic and kinematic hardening pre-  
222 dictions (Section 4.1). Results are obtained for pure mode I, pure mode II  
223 and mixed-mode steady-state crack propagation. Secondly, the origin of the  
224 notable differences observed in the shielding ratio is investigated through the  
225 energy dissipation density in the isotropic and kinematic hardening materials  
226 (Section 4.2). The energy dissipation density is investigated in an attempt  
227 to identify which regions of the active plastic zone in the vicinity of the crack  
228 tip that primarily controls shielding by adding to the steady-state fracture  
229 toughness. This investigation is conducted by tracing material points travel-  
230 ing along the crack path (in the  $x_1$ -direction) at different distances from the  
231 crack face.

232 The study employs a mesh with a total of 310,000 elements in the entire  
233 domain, where approximately 60,000 of the elements are located in the region  
234 of the main plastic zone. Furthermore, the critical normal and tangential  
235 separation will be related to the mesh such that;  $\delta_n^c = \delta_t^c = 0.2L_{e,\min}$ , where  
236  $L_{e,\min}$  is the minimum element length in the domain.

### 237 4.1. Crack tip shielding ratio

238 To quantify the differences between isotropic and kinematic hardening,  
239 the shielding ratio,  $K_{ss}/K_0$ , is studied by employing the cohesive zone model  
240 presented in Section 3.1. The cohesive zone model ensures that the energy  
241 release rate required for crack propagation is identical for both the isotropic  
242 and kinematic material while the far-field is scaled accordingly.

243 The crack tip shielding ratio,  $K_{ss}/K_0$ , is presented as a function of the  
244 normalized peak traction,  $\hat{\sigma}/\sigma_y$ , in Fig. 5 for a pure mode I crack ( $K_{II} = 0$ )  
245 for both isotropic (dashed lines) and kinematic hardening (solid lines). For  
246 low hardening ( $E_t = E/100$ ) it is seen that the shielding ratio is almost iden-  
247 tical for the two materials as hardening has limited influence on the predicted

248 stress level (close to perfectly plastic). That is, the yield surface remains close  
 249 to identical for the two types of material hardening. However, a significant  
 250 shift is seen for the isotropic model when the strain hardening is increased  
 251 to  $E_t = E/20$ , while the effect in the kinematic model is small. Similarly,  
 252 by choosing an even higher hardening,  $E_t = E/10$ , an even greater shift is  
 253 seen for the isotropic material, whereas the shift for the kinematic material  
 254 is much less pronounced. It is important to notice that for fixed strain hard-  
 255 ening and peak traction in the cohesive zone, the kinematic material always  
 256 predicts either an equal or greater shielding ratio compared to that of the  
 257 isotropic material model. Furthermore, it is seen that shield ratio for the  
 258 kinematic hardening solid appears to be unbounded for peak tractions larger  
 259 than 2.9, 3.2 and 4.4 times the yield stress for  $E_t = E/100$ ,  $E_t = E/20$  and  
 260  $E_t = E/10$ , respectively.

261 The shielding ratio for a pure mode II loaded crack ( $K_I = 0$ ) is presented  
 262 in Fig. 6. Contrary to the pure mode I crack, a much less significant effect is  
 263 observed when changing from an isotropic to a kinematic hardening model.  
 264 As expected, the curves are almost identical for the case of  $E_t = E/100$   
 265 (and essentially coincides in the figure), but the difference in the predicted  
 266 shielding ratio remains limited when increasing the strain hardening. When  
 267 compared to the mode I study, it is also observed that similar values of the  
 268 steady-state fracture toughness are attained for significantly lower cohesive  
 269 strengths. The reason for this is that the stress triaxiality close to the crack  
 270 tip is significantly smaller in mode II, promoting plastic deformation at lower  
 271 load levels, as specified in terms of the stress intensity factor. Furthermore,  
 272 as discussed by Tvergaard [5], values in closer agreement between mode I  
 273 and mode II would be attained if the crack was allowed to grow along its  
 274 preferred path.

275 Finally, the shielding ratio is studied for the mixed mode case where  
 276  $K_I = K_{II}$ . Figure 7 reveals a shielding ratio for mixed mode conditions  
 277 which is located between the pure mode I and pure mode II predictions.  
 278 However, it should be noted that the contribution from each mode in an  
 279 elastic-plastic solid relies on the crack tip conditions and is therefore not  
 280 directly reflected by the far-field mode mixity.

#### 281 *4.2. Active plastic zones and energy dissipation*

282 The investigation of steady-state fracture toughness showed a larger shield  
 283 ratio for kinematic hardening solids, independently of the loading mode. To  
 284 assess the influence on the material behavior in the vicinity of the crack

285 tip, the plastic zone is presented in Fig. 8 for both isotropic and kinematic  
 286 hardening for the mode I case with tangent modulus  $E_t = E/20$  and peak  
 287 traction  $\hat{\sigma}/\sigma_y = 3.5$ . As expected, the plastic zone is significantly larger in  
 288 the kinematic hardening case to accommodate the larger dissipation.

289 The different energy dissipation levels in the two hardening models are  
 290 investigated through the plastic zone shapes and the associated energy dis-  
 291 sipation densities by applying identical far-field loading conditions (equal  
 292 energy input to the system) in the two models. A direct consequence of this  
 293 study is that the energy at the crack tip depends on the energy dissipation  
 294 in each model, i.e. the fracture criterion is not identical. For this study, the  
 295 cohesive elements are removed from the model i.e. the crack plane is now  
 296 represented by a line of single nodes rather than dual nodes such that crack  
 297 tip opening does not take place and the crack remains perfectly sharp. The  
 298 level of hardening remains fixed at  $E_t = E/20$ . Furthermore, in the study of  
 299 the plastic zones, any length quantity is normalized by Irwin's approxima-  
 300 tion of the plastic zone size  $R_p$ , identical to Eq. (3), but with the far-field,  
 301  $K$ , instead of the initiation threshold  $K_0$  (similarly,  $\Gamma$  is computed from the  
 302 far-field,  $K$ ).

303 The active plastic zones for pure mode I and mode II loading are presented  
 304 in Fig. 9. For a mode I crack (see Fig. 9a), the effect of the kinematic model  
 305 is most pronounced close to the crack tip - especially on the downstream  
 306 side (left in Fig. 9) of the primary active plastic zone where the material  
 307 experiences reversed loading. The isotropic model is dominant, in terms  
 308 of the width of the active plastic zone, further away from the crack face  
 309 on the upstream side (right in Fig. 9). For the mode II loaded crack (see  
 310 Fig. 9b), no significant differences between the plastic zone for the isotropic  
 311 and kinematic hardening models are observed, consistent with the shielding  
 312 ratio study. This is largely tied to the nature of a mode II loaded crack  
 313 tip as reversed loading is absent and the non-proportionality is less severe  
 314 compared to the mode I crack.

315 To further investigate the differences between the two hardening models,  
 316 the energy dissipation density,  $w$ , is extracted along the four horizontal paths  
 317 illustrated in Fig. 9. On each path, the energy dissipation density is evaluated  
 318 as;

$$w = - \int_{-\infty}^{\infty} \left( \sigma_{ij} \frac{d\varepsilon_{ij}^p}{dx_1} \right) dx_1, \quad (29)$$

319 according to the streamline integration scheme. The energy dissipation den-

320 sity is presented in Fig. 10 for mode I loading. Here, it is seen that energy  
 321 dissipation density continuously grows from the onset of the plastic zone un-  
 322 til the steady-state level is reached far behind the crack tip. Common to  
 323 all paths is that the kinematic hardening entails a larger energy dissipation  
 324 density. The largest difference is seen closest to the crack plane (path 1) in  
 325 the unloading region immediately behind the crack tip where the kinematic  
 326 model dissipates more energy than the isotropic model. The kinematic model  
 327 continues to have the largest dissipation density for path 2 and 3 albeit the  
 328 difference becomes progressively smaller when moving away from the crack  
 329 plane as the loading becomes less complex and less severe, affecting both  
 330 the level of plasticity and the non-proportionality. The trend is, however, in-  
 331 verted for path 4 as the isotropic solution here displays the largest dissipation  
 332 density. Nevertheless, the magnitude of the energy dissipation density in this  
 333 region is comparably low and has little influence on the overall dissipation.

334 To identify possible sources of the difference in the energy dissipation  
 335 density for a mode I loaded crack, the translation of the kinematic yield  
 336 surface is investigated. The translation of the kinematic yield surface is  
 337 represented by the effective back stress;

$$\alpha_e = \sqrt{3\alpha'_{ij}\alpha'_{ij}/2}. \quad (30)$$

338 In Fig. 11 it is seen that for path 1 and 2 (see Fig. 9a), the yield surface con-  
 339 tinues to translate in stress space as reversed plasticity takes place behind  
 340 the crack tip. Ultimately, the effective back stress profile reaches a short  
 341 unloading plateau further behind the crack tip. This continued movement of  
 342 the kinematic yield surface causes additional dissipation when compared to  
 343 the isotropic model. As non-proportional loading or reversed plasticity takes  
 344 place the kinematic hardening solid experiences a greater change to the yield  
 345 surface normal (larger curvature compared to the expanded isotropic yield  
 346 surface) and hence the plastic strain increment undergoes a larger change in  
 347 direction (or magnitude). In fact, this observation is partially supported by  
 348 Tvergaard [32], investigating sheet metal necking using a kinematic harden-  
 349 ing model. Here, the kinematic hardening was observed to promote localiza-  
 350 tion (similar to corner theories, see Mear and Hutchinson [33]) due to the  
 351 curvature of the kinematic yield surface. This suggests that non-proportional  
 352 loading has a significant impact in a kinematic model. For path 3 and 4, it is  
 353 seen that the back stress reaches a constant value directly due to the absence

354 of reversed plasticity in these regions. This observation, combined with less  
355 severe non-proportionality of the loading in this region, supports the smaller  
356 difference in dissipation density observed in Fig. 10.

357 In contrast to the mode I loaded crack, the difference in the dissipation  
358 density is negligible when comparing an isotropic and a kinematic hardening  
359 material for a mode II loaded crack. Figure 12 shows results along the four  
360 paths shown in Fig. 9b. For path 1, the dissipation density is slightly higher  
361 for isotropic hardening, whereas for path 2, 3, and 4 the energy dissipation  
362 density is slightly higher for the kinematic model. Thus, for the mode II  
363 crack, differences are marginal and no distinct region is observed where one  
364 model clearly dominates.

365 The effective back stress along the four paths in Fig. 9b is shown in  
366 Fig. 13. Here it is seen that the yield surface translates in the stress space  
367 until the crack tip is reached and remains stationary (constant  $\alpha_e$ ) behind  
368 the crack. That is, no reversed plasticity is predicted for the mode II loaded  
369 crack, effectively eliminating one source of additional energy dissipation in  
370 the kinematic hardening model relative to the mode I analysis. In addition,  
371 the non-proportional loading is expected to be much less severe for the mode  
372 II crack, rationalizing the similar steady-state fracture toughness predictions  
373 obtained with isotropic and kinematic hardening models, respectively, (recall  
374 Fig. 6).

## 375 5. Concluding remarks

376 A steady-state framework combined with a cohesive zone model has been  
377 developed for the purpose of studying the difference in cracks propagating  
378 in either isotropic or kinematic hardening materials. The study focuses on  
379 the plastic zone size, the evolution of the strain energy dissipation density,  
380 and the shielding ratio for mode I, mode II and mode I/II cracks. The main  
381 findings are:

- 382 • The shielding ratio is generally largest for the kinematic hardening  
383 material compared to an isotropic hardening material. The effect is  
384 most significant for a mode I crack whereas the effect is very limited for  
385 a mode II crack. Under mixed mode loading conditions, the shielding  
386 ratio falls between that of the two pure modes.
- 387 • The active plastic zone for a mode I crack is slightly larger for a kine-  
388 matic hardening material in the central half of the active plastic zone,

389 whereas the isotropic hardening material has a larger plastic zone in  
390 the exterior half of the active plastic zone, for identical far-field loading.  
391 For the mode II crack, there is no significant difference in the plastic  
392 zone shapes.

- 393 • The largest difference in energy dissipation density between the isotropic  
394 and kinematic hardening material for a mode I crack is observed close  
395 to the crack face, behind the crack tip, in the region of reverse loading.  
396 For the mode II crack, a very small difference in the dissipation density  
397 is observed. The dissipation density is slightly larger close to the crack  
398 face for isotropic hardening whereas further away from the crack face  
399 the kinematic model becomes dominant. The difference is, however,  
400 very small.

401

402 The main sources of the larger energy dissipation for kinematic harden-  
403 ing is attributed to the stronger path dependence associated with a larger  
404 curvature of the yield surface (sensitivity to non-proportional loading) and  
405 the reverse loading prone to initiate plasticity sooner than for the isotropic  
406 hardening material (smaller yield surface). The large differences observed in  
407 mode I conditions between isotropic and kinematic predictions imply that  
408 fracture toughness estimations from R-curve modeling are very conservative.  
409 This could have important implications in damage tolerant design in the  
410 aerospace or energy sectors, among others.

## 411 **6. Acknowledgement**

412 The work is financially supported by The Danish Council for Independ-  
413 ent Research in the project “New Advances in Steady-State Engineering  
414 Techniques”, grant DFF-4184-00122. E. Martínez-Pañeda additionally ac-  
415 knowledges financial support from the Ministry of Economy and Compet-  
416 itiveness of Spain through grant MAT2014-58738-C3 and the People Pro-  
417 gramme (Marie Curie Actions) of the European Unions Seventh Framework  
418 Programme (FP7/2007-2013) under REA grant agreement n 609405 (CO-  
419 FUNDPstdocDTU).

420 **References**

- 421 [1] A. G. Varias, C. F. Shih, Quasi-static crack advance under a range of  
422 constraints - steady-state fields based on a characteristic length, *Journal*  
423 *of the Mechanics and Physics of Solids* 41 (5) (1993) 835–861.
- 424 [2] V. Tvergaard, J. W. Hutchinson, The influence of plasticity on mixed-  
425 mode interface toughness, *Journal of the Mechanics and Physics of Solids*  
426 41 (6) (1993) 1119–1135.
- 427 [3] Z. Suo, C. F. Shih, A. G. Varias, A theory for cleavage cracking in the  
428 presence of plastic flow, *Acta Metall Mater* 41 (1993) 1551–7.
- 429 [4] H. Cleveringa, E. Van der Giessen, A. Needleman, A discrete dislocation  
430 analysis of mode I crack growth, *Journal of the Mechanics and Physics of*  
431 *Solids* 48 (67) (2000) 1133–1157.
- 432 [5] V. Tvergaard, Effect of pure mode i, ii or iii loading or mode mixity  
433 on crack growth in a homogeneous solid, *International Journal of Solids*  
434 *and Structures* 47 (11-12) (2010) 1611–1617.
- 435 [6] K. L. Nielsen, C. F. Niordson, J. W. Hutchinson, Strain gradient effects  
436 on steady-state crack growth in rate-dependent materials, *Eng. Fract.*  
437 *Mech.* 96 (2012a) 61–71.
- 438 [7] K. L. Nielsen, C. F. Niordson, Rate sensitivity of mixed mode interface  
439 toughness of dissimilar metallic materials: Studied at steady state, *Int.*  
440 *J. Solids Struct.* 49 (2012b) 576–583.
- 441 [8] Y. Jiang, Y. Wei, J. R. Smith, J. W. Hutchinson, A. G. Evans, First  
442 principles based predictions of the toughness of a metal/oxide interface,  
443 *International Journal of Materials Research* 101 (2010) 1–8.
- 444 [9] K. J. Juul, K. L. Nielsen, C. F. Niordson, Steady-state crack growth in  
445 single crystals under mode i loading, *J. Mech. Phys. Solids* 101 (2017)  
446 209–222.
- 447 [10] C. M. Landis, T. Pardoen, J. W. Hutchinson, Crack velocity dependent  
448 toughness in rate dependent materials, *Mechanics of Materials* 32 (11)  
449 (2000) 663–678.

- 450 [11] V. Tvergaard, J. W. Hutchinson, The relation between crack-growth  
451 resistance and fracture process parameters in elastic plastic solids, *Journal of the Mechanics and Physics of Solids* 40 (6) (1992) 1377–1397.  
452 doi:10.1016/0022-5096(92)90020-3.  
453
- 454 [12] Y. Wei, J. W. Hutchinson, Steady-state crack growth and work of fracture for solids characterized by strain gradient plasticity, *J. Mech. Phys. Solids* 45 (1997) 1253–73.  
455  
456
- 457 [13] E. Martínez-Pañeda, C. F. Niordson, On fracture in finite strain gradient plasticity, *International Journal of Plasticity* 80 (2016) 154–167.  
458
- 459 [14] L. B. Freund, J. W. Hutchinson, High strain-rate crack growth in rate-dependent plastic solids, *Journal of the Mechanics and Physics of Solids* 33 (2) (1985) 169–191.  
460  
461
- 462 [15] H. C. Cao, A. G. Evans, An experimental-study of the fracture-resistance of bimaterial interfaces, *Mechanics of Materials* 7 (4) (1989) 295–304. doi:10.1016/0167-6636(89)90020-3.  
463  
464
- 465 [16] V. Tvergaard, Theoretical investigation of the effect of plasticity on crack growth along a functionally graded region between dissimilar elastic-plastic solids, *Engineering Fracture Mechanics* 69 (14-16) (2002) 1635–1645. doi:10.1016/S0013-7944(02)00051-6.  
466  
467  
468
- 469 [17] S. Kumar, W. A. Curtin, Crack interaction with microstructure, *Materials Today* 10 (9) (2007) 34–44.  
470
- 471 [18] E. Martínez-Pañeda, N. A. Fleck, Crack growth resistance in metallic alloys: the role of isotropic versus kinematic hardening, *Journal of Applied Mechanics* 85 (2018) 11002 (6 pages). arXiv:1806.08986.  
472  
473
- 474 [19] M. F. Ashby, The deformation of plastically non-homogeneous materials, *Philosophical Magazine* 21 (170) (1970) 399–424. arXiv:9809069v1, doi:10.1080/14786437008238426.  
475  
476
- 477 [20] C. de Formanoir, A. Brulard, S. Vives, G. Martin, F. Prima, S. Michotte, E. Riviere, A. Dolimont, S. Godet, A strategy to improve the work-hardening behavior of ti-6al-4v parts produced by additive manufacturing, *Materials Research Letters* 5 (3) (2017) 201–208.  
478  
479  
480

- 481 [21] P. B. Woelke, M. D. Shields, J. W. Hutchinson, Cohesive  
482 zone modeling and calibration for mode I tearing of large duc-  
483 tile plates, *Engineering Fracture Mechanics* 147 (2015) 293–305.  
484 doi:10.1016/j.engfracmech.2015.03.015.
- 485 [22] R. G. Andersen, C. L. Felter, K. L. Nielsen, Micro-mechanics based  
486 cohesive zone modeling of full scale ductile plate tearing: From initiation  
487 to steady-state, (submitted for publication).
- 488 [23] R. H. Dean, J. W. Hutchinson, Quasi-static steady crack growth in  
489 small-scale yielding, *Fracture Mechanics: Twelfth Conference, ASTM*  
490 *STP700*, American Society for Testing and Materials (1980) 383–405.
- 491 [24] M. L. Williams, On the stress distribution at the base of a stationary  
492 crack, *J. App. Mech.* 24 (1957) 109–114.
- 493 [25] J. Lemaitre, J.-L. Chaboche, *Mechanics of solid materials*, Cambridge  
494 University Press, New York, 1990.
- 495 [26] H. Ziegler, A modification of pragers hardening rule, *Quarterly of Ap-*  
496 *plied Mathematics* 17 (1) (1959) 55–65. doi:10.1090/qam/104405.
- 497 [27] K. J. Juul, K. L. Nielsen, C. F. Niordson, Steady-state numerical mod-  
498 eling of size effects in micron scale wire drawing, *J. Manuf. Process.* 25  
499 (2017) 163–171.
- 500 [28] C. F. Niordson, Analysis of steady-state ductile crack growth along a  
501 laser weld, *Int. J. Frac.* 111 (2001) 53–69.
- 502 [29] S. del Busto, C. Betegon, E. Martínez-Pañeda, A cohesive zone frame-  
503 work for environmentally assisted fatigue, *Engineering Fracture Mechan-*  
504 *ics* 185 (2017) 210–226. doi:10.1016/j.engfracmech.2017.05.021.
- 505 [30] J. Segurado, J. LLorca, A new three-dimensional interface finite element  
506 to simulate fracture in composites, *Int. J. Solids and Struct.* 41 (2004)  
507 2977–2993.
- 508 [31] E. Martínez-Pañeda, S. del Busto, C. Betegon, Non-local plasticity ef-  
509 fects on notch fracture mechanics, *Theor. Appl. Fract. Mech.* 92 (2017)  
510 276–287.

- 511 [32] V. Tvergaard, Effect of kinematic hardening on localized necking in  
512 biaxially stretched sheets, *Int J Mech Sci* 20 (9) (1978) 651–658.
- 513 [33] M. E. Mear, J. W. Hutchinson, Influence of yield surface curvature on  
514 flow localization in dilatant plasticity, *Mechanics of Materials* 4 (1985)  
515 395–407.
- 516 [34] V. Tvergaard, *Plasticity and creep in structural materials*, Polyteknisk  
517 Kompendie, 2001.

518 **List of Figures**

519	1	Mode I/II crack growth at steady-state with an embedded	
520		cohesive zone in the path of the crack. . . . .	25
521	2	Traction separation relation governing the cohesive zone. . . .	26
522	3	Evolution of yield surface for (a) isotropic hardening and (b)	
523		kinematic hardening (Tvergaard [34]). . . . .	27
524	4	Illustration of linked nodes in the control algorithm. . . . .	28
525	5	Shielding ratio for a mode I loaded crack ( $K_{II} = 0$ ) propa-	
526		gating in isotropic and kinematic hardening materials, respec-	
527		tively, at various peak tractions, $\hat{\sigma}$ , and tangent modulus, $E_t$ . .	29
528	6	Shielding ratio for mode II loaded crack ( $K_I = 0$ ) propagating	
529		in an isotropic and a kinematic hardening material, respec-	
530		tively, at various peak tractions, $\hat{\sigma}$ , and tangent modulus, $E_t$ . .	30
531	7	Shielding ratio for mixed mode I/II loaded crack ( $K_I = K_{II}$ )	
532		propagating in an isotropic and kinematic hardening material,	
533		respectively, at various peak tractions and tangent modulus. .	31
534	8	Active plastic zones for isotropic and kinematic hardening with	
535		$E_t = E/20$ and $\hat{\sigma}/\sigma_y = 3.5$ for pure mode I. . . . .	32
536	9	Active plastic zones for isotropic and kinematic hardening in	
537		the absence of the cohesive zone with $E_t = E/20$ . Here for;	
538		a) pure mode I, and b) pure mode II. The horizontal lines	
539		illustrate the paths along which the energy dissipation density	
540		has been extracted. The paths 1, 2, 3, and 4 are located at	
541		the heights; $x_2/R_p = 0.05, 0.15, 0.3, 0.7$ , respectively. . . . .	33
542	10	Mode I energy dissipation density in the absence of the co-	
543		hesive zone for isotropic and kinematic hardening, and the	
544		difference between the models, with $E_t = E/20$ . . . . .	34
545	11	Effective back stress in the absence of the cohesive zone for	
546		kinematic hardening with $E_t = E/20$ . . . . .	35
547	12	Mode II energy dissipation density in the absence of the co-	
548		hesive zone for isotropic and kinematic hardening, and the	
549		difference between the models, with $E_t = E/20$ . . . . .	36
550	13	Effective back stress in the absence of the cohesive zone for	
551		kinematic hardening with $E_t = E/20$ . . . . .	37

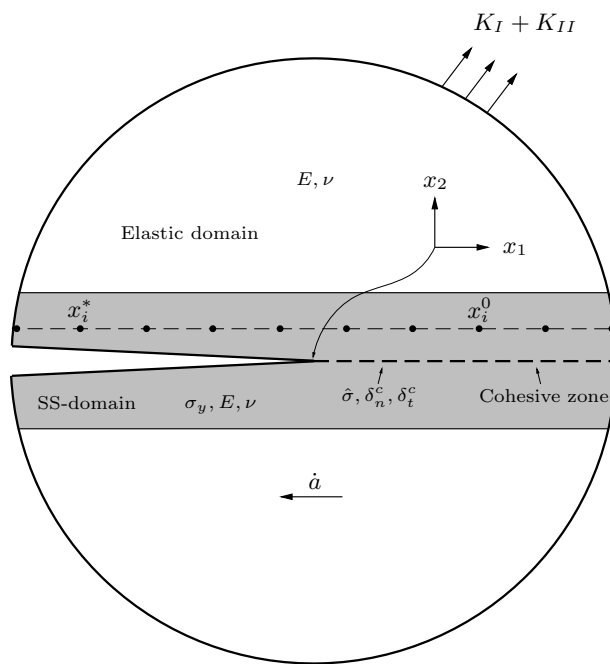


**Figure 1:** Mode I/II crack growth at steady-state with an embedded cohesive zone in the path of the crack.

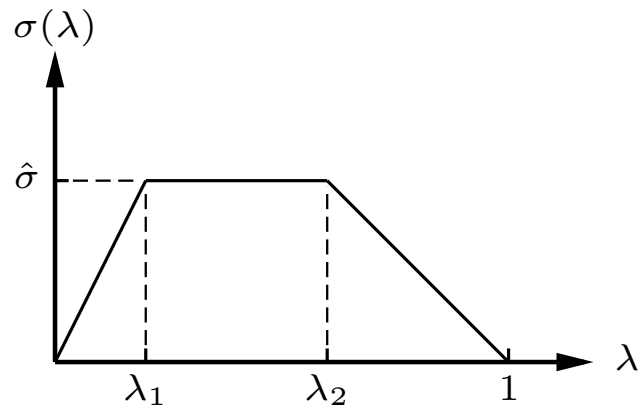


**Figure 2:** Traction separation relation governing the cohesive zone.

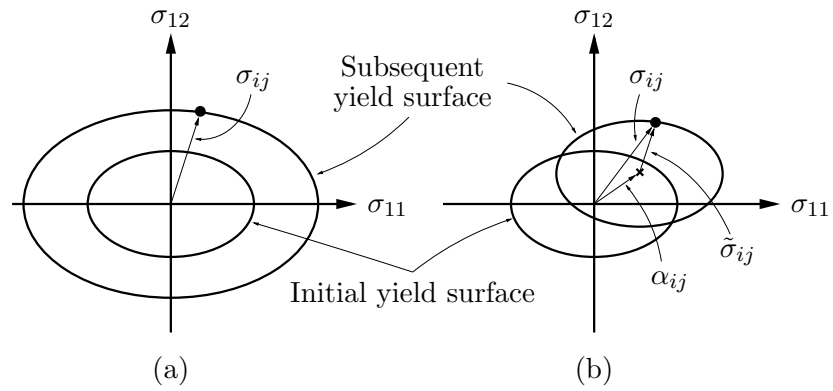


**Figure 3:** Evolution of yield surface for (a) isotropic hardening and (b) kinematic hardening (Tvergaard [34]).

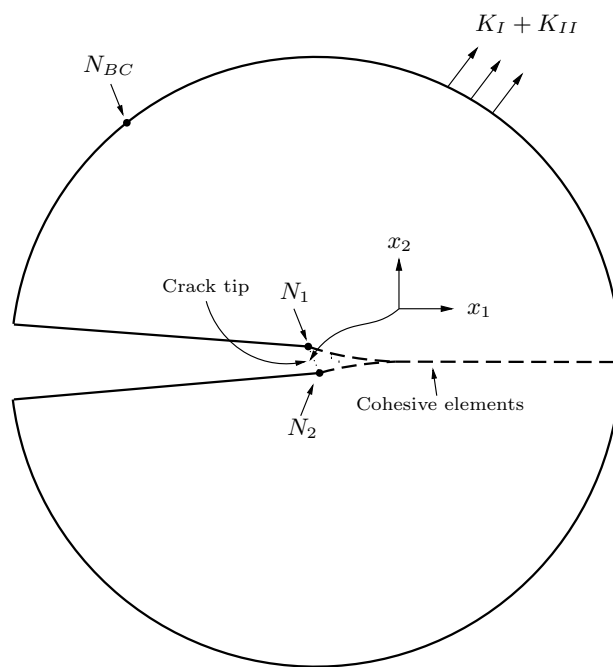


**Figure 4:** Illustration of linked nodes in the control algorithm.

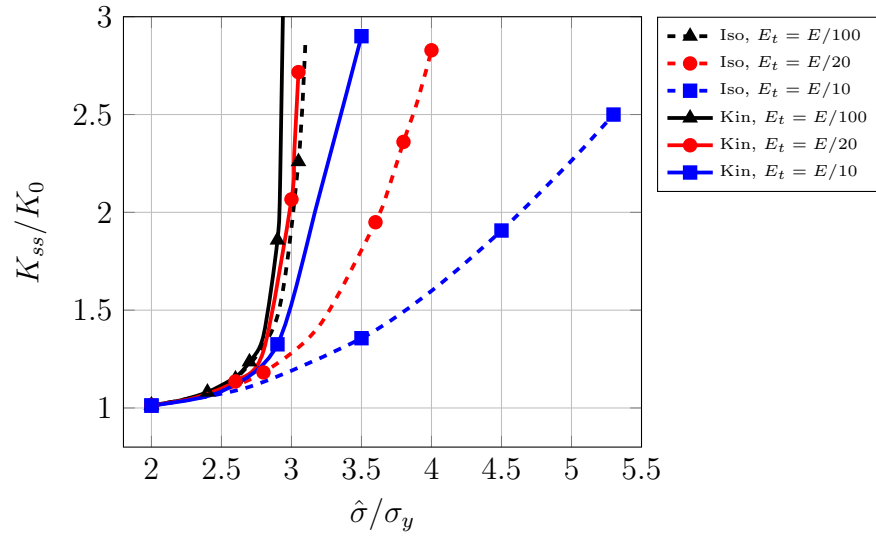


**Figure 5:** Shielding ratio for a mode I loaded crack ( $K_{II} = 0$ ) propagating in isotropic and kinematic hardening materials, respectively, at various peak tractions,  $\hat{\sigma}$ , and tangent modulus,  $E_t$ .

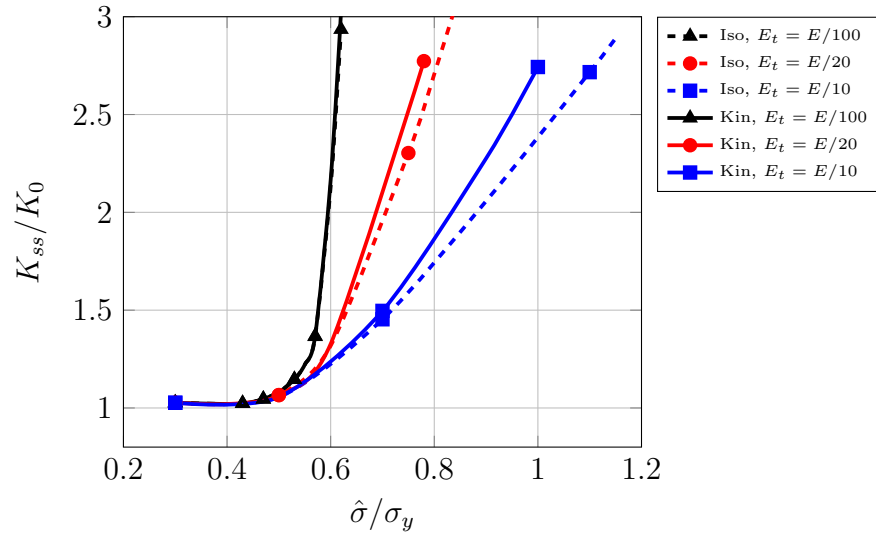


**Figure 6:** Shielding ratio for mode II loaded crack ( $K_I = 0$ ) propagating in an isotropic and a kinematic hardening material, respectively, at various peak tractions,  $\hat{\sigma}$ , and tangent modulus,  $E_t$ .

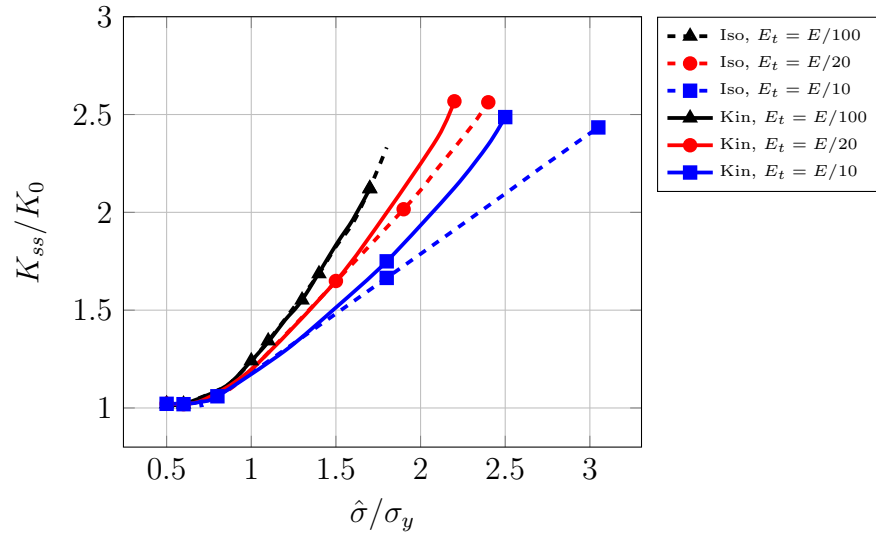


**Figure 7:** Shielding ratio for mixed mode I/II loaded crack ( $K_I = K_{II}$ ) propagating in an isotropic and kinematic hardening material, respectively, at various peak tractions and tangent modulus.

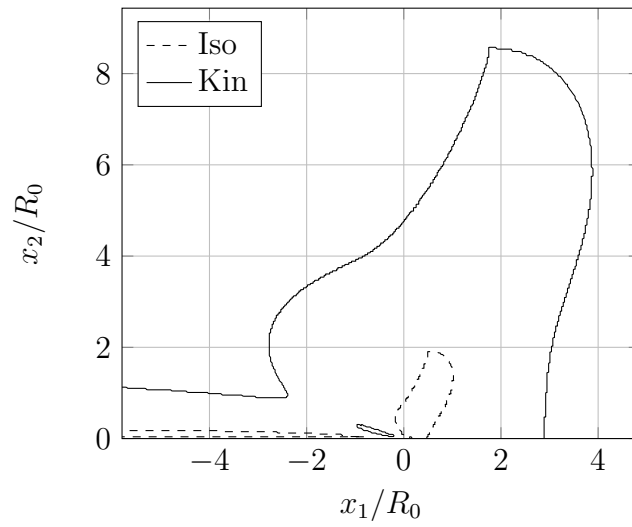


**Figure 8:** Active plastic zones for isotropic and kinematic hardening with  $E_t = E/20$  and  $\hat{\sigma}/\sigma_y = 3.5$  for pure mode I.

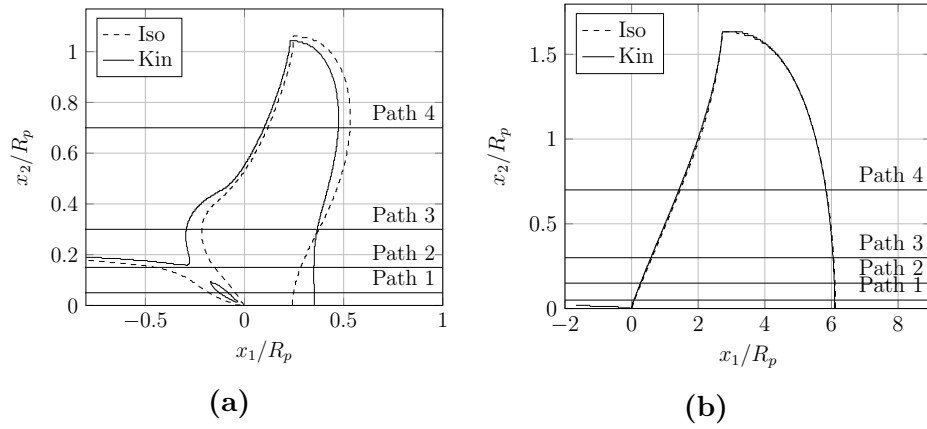


**Figure 9:** Active plastic zones for isotropic and kinematic hardening in the absence of the cohesive zone with  $E_t = E/20$ . Here for; a) pure mode I, and b) pure mode II. The horizontal lines illustrate the paths along which the energy dissipation density has been extracted. The paths 1, 2, 3, and 4 are located at the heights;  $x_2/R_p = 0.05, 0.15, 0.3, 0.7$ , respectively.

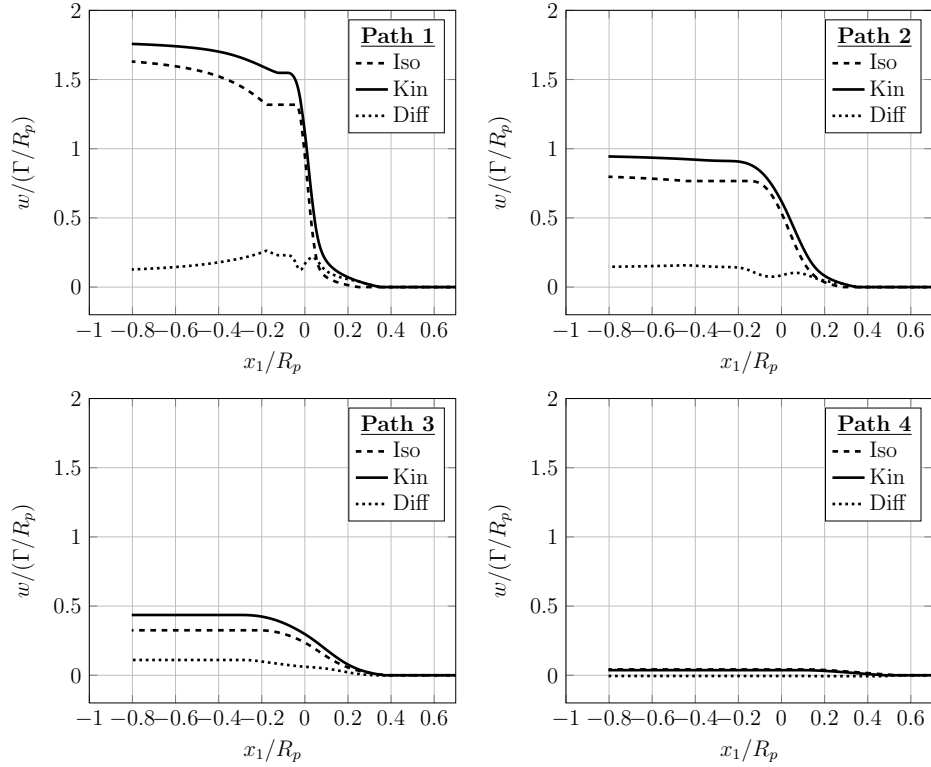


**Figure 10:** Mode I energy dissipation density in the absence of the cohesive zone for isotropic and kinematic hardening, and the difference between the models, with  $E_t = E/20$ .

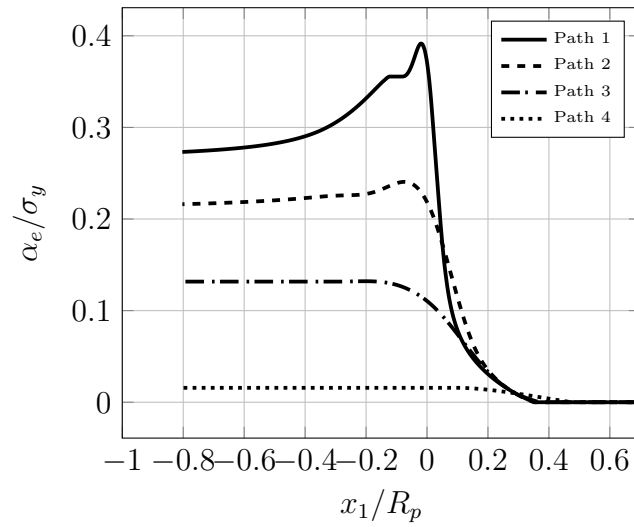


**Figure 11:** Effective back stress in the absence of the cohesive zone for kinematic hardening with  $E_t = E/20$ .

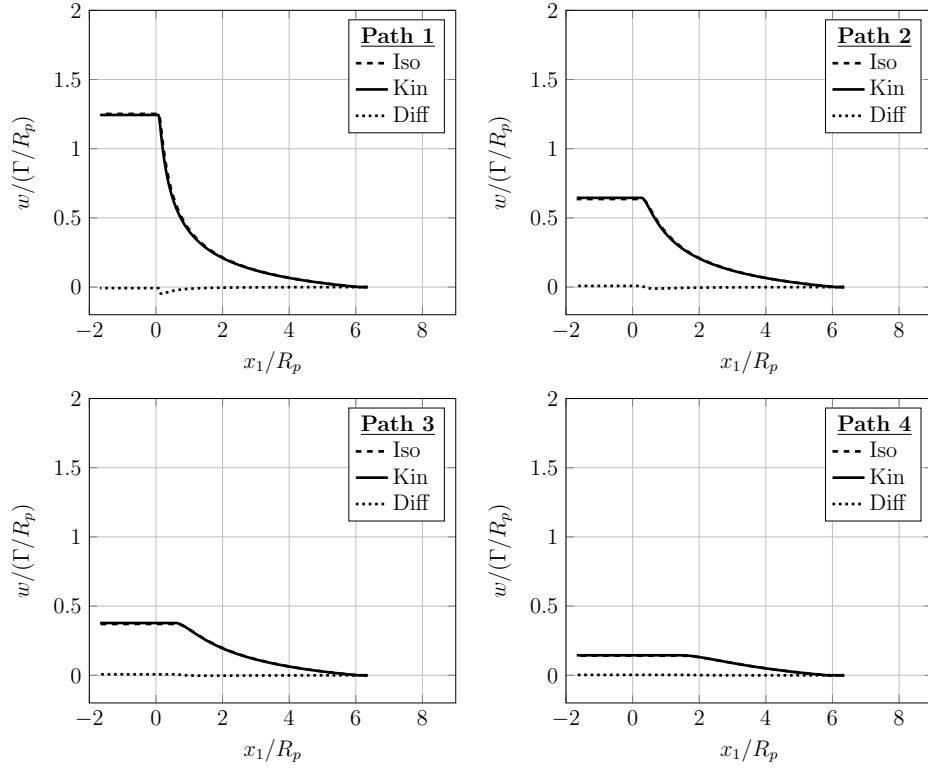


**Figure 12:** Mode II energy dissipation density in the absence of the cohesive zone for isotropic and kinematic hardening, and the difference between the models, with  $E_t = E/20$ .

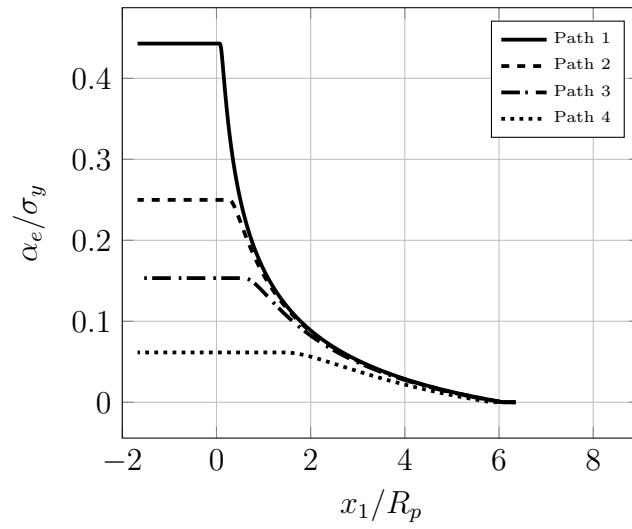


**Figure 13:** Effective back stress in the absence of the cohesive zone for kinematic hardening with  $E_t = E/20$ .

552 **List of Tables**

553     1    Material Properties. . . . . 39

Parameter	Significance	Value
$\sigma_y/E$	Yield strain	0.003
$\hat{\sigma}$	Peak normal traction	$0.3 - 5.3\sigma_y$
$\nu$	Poisson's ratio	0.33
$E/E_t$	Tangent modulus	10 – 100
$\lambda_1$	Shape parameter	0.15
$\lambda_2$	Shape parameter	0.5

**Table 1:** Material Properties.